eprints@whiterose.ac.uk
https://eprints.whiterose.ac.uk/

Microstructure development and mechanical performance of Al₂CrFeMnTi light-weight high entropy alloy

Hadi Jahangiri [a]*, Samira Mohagheghi [b], Armin Asghari Alamdari [a,c], Rifat Yilmaz [d], Kübra Gürcan Bayrak [d], Feng YU [e], Hassan Ghadbeigi [e], Erhan Ayas [d], Amir Motallebzadeh [a]

[a] Koç University Surface Science and Technology Center (KUYTAM), Sariyer, 34450 Istanbul, Turkey
[b] Department of Mechanical Engineering, Istinye University, Zeytinburnu 34010, Istanbul, Turkey
[c] Materials Science and Engineering, Koç University, Sariyer 34450, Istanbul, Turkey
[d] Department of Materials Science and Engineering, Eskişehir Technical University, Eskişehi, 26555, Turkey
[e] Department of Mechanical Engineering, Sir Frederick Mappin Building, the University of Sheffield, Mappin Street, S1 3JD Sheffield, UK

Abstract

Light-weight high entropy alloys (LWHEAs) are considered equiatomic or near-equiatomic alloys consisting of at least five elements. Low-density elements, like Al and Ti, are the key constituents in designing these alloys so that features such as reduced overall density and improved mechanical properties are achieved.

A new LWHEAs (Al₂CrFeMnTi) is designed, where mechanical alloying followed by subsequent casting is carried out for a successful synthesis. As a result, chemically homogenous samples are fabricated that possess a multiphase microstructure of BCC solid solution, C_{14} Laves phase, and $L2_1$ precipitates in the as-cast state. Although the presence of intermetallic phases results in high hardness characterized by nanoindentation tests, the produced alloy demonstrates some level of ductility before failure. This behavior could be linked to the minimal strain hardening of the BCC phase. Additionally, the formation of ultra-fine $L2_1$ precipitates within the BCC phase is contributed to the high strength and the modified strain observed in the alloy.

Keywords: High entropy alloys, Intermetallic, Microstructure, Mechanical properties, Nanoindentation

1. Introduction

The design and fabrication of high entropy alloys (HEAs) have attracted substantial attention within the research community since the proposal of the equiatomic multicomponent alloy concept [1]. In sharp contrast to conventional alloys, HEAs contain a high concentration of at least five elements varying in the range of 5 to 35 at % [2, 3]. Four main design concepts, namely high configurational entropy, sluggish diffusion kinetics, severe lattice distortion, and cocktail effect, commonly describe HEAs [3]. The high entropy effect in HEAs can facilitate the formation of solid-solution phases over complex intermetallic phases. Consequently, solid solution hardening [4] is known to be the principal strengthening mechanism and contributes to the exceptional mechanical properties of these single-phase HEAs [5]. Although researchers have tried to develop single-phase alloys, the majority of HEAs include multiphase solid solutions and intermetallics (IMs) in which complex strengthening mechanisms occur as a result of multiphase solid solutions [6]. The formation of intermetallic phases in addition to the solid solution phase has also been reported in low and medium entropy alloys, such as $Al_x(LiMgCuZn)_{100-x}$ [7].

On the other hand, while the IMs are capable of improving the performance of the alloys at higher temperatures, their mechanical properties are negatively affected at room temperature due to their excessive brittleness. Therefore, many attempts have been made to develop new alloys with embedded IMs for high-temperature applications [8]. For instance, the design of a triplex microstructure, which includes two intermetallic phases in an FCC solid solution phase, is reported to be a paradigm shift from the known inverse relationship between strength and ductility. An excellent strength-ductility combination was achieved in $Al_{0.3}CoCrFeNi$ high entropy alloy [9]. In this context, the precipitation hardening mechanism can be promoted by the formation of ultrafine IMs leading to higher yield, ultimate tensile strength, and enhanced microhardness in HEAs [10, 11]. In addition, the introduction of the eutectic concept in the design of HEAs brings a new prospect, which combines the advantages of solid solution and intermetallic phases, to achieve a high hardness and softening resistance at elevated temperatures; these improvements are originated from the uniform and fine lamellar eutectic microstructure [12].

A new generation of HEAs with enhanced mechanical properties has already been developed while their density and the total weight of the components has been reduced. Accordingly, this progress results in the production of light-weight high entropy alloys (LWHEAs) where Ti, Mg, Al, Li, Si, and Ca are the primary constituent elements [13]. There have been some efforts to develop Al/Ti-based LWHEAs in which these elements stabilize the formation of IMs while

reducing the overall density of the alloy [13]. Although the development of new LWHEAs for industrial applications can be considered as a valuable research area, extensive studies are required to unveil the role of constitutive phases in the microstructure and resulting mechanical properties; this issue can be considered very challenging due to the vast compositional variations that can be achieved by these alloys [14]. Even though alloy design relies on thermodynamic databases, the compositional variation of LWHEAs is limited and constantly improving [14]. Therefore, empirical investigation of the microstructures formed in these alloys and their contributions to mechanical and functional properties are essential steps towards future developments. Moreover, implementing the machine-learning approach will significantly facilitate the design of new alloys and predict the microstructure. For instance, the machine-learning approach has already been applied to determine all eutectic compositions in the Al-Co-Cr-Fe-Ni system [15]. The next step certainly would be providing a link between the microstructures and properties.

In an LWHEA alloy based on Ni, *i.e.,* Ni-Cr-Co-Ti-V-Al system, it is suggested that Al promotes the formation of body-centered-cubic (BCC) phase which has high stability at elevated temperature and promotes the alloy's potential for high-temperature applications [16]. On the other hand, the addition of Ti to the Al-Co-Cr-Cu-Fe-Ni system stabilizes intermetallic phases due to high negative mixing enthalpy between Ti and other elements [17]. By replacing the expensive and common Ni and Co elements with cost-effective Al and Ti, the Al-Cr-Fe-Mn-Ti system becomes a suitable candidate for designing LWHEAs. Moreover, the presence of Al and Cr can contribute to increment of oxidation and corrosion resistance which can lead to possible applications in harsh corrosive environments. The presence of other inexpensive elements such as Fe, Mn, and Cr not only reduces the cost of producing but also contributes to solid solution strengthening of the alloy, as reported in [18].

The present research aims to take up the early work by Feng *et al*. [18] on $Al_{1.5}CrFeMnTi$ to characterize the microstructural features of non-equiatomic as-cast $Al_2CrFeMnTi$ alloy and determine its mechanical behavior. Alloys of this class, such as $Al_xCrFeMnTi_y$ [6, 8], possess a multiphase system in their as-cast state, and thus, the overall mechanical behavior is affected by different hardening mechanisms. The results show that the as-cast microstructure of $Al_2CrFeMnTi$ alloy consists of the BCC solid-solution, C_{14} Laves phase, and ultra-fine $L2_1$ precipitates. The alloy exhibits a plastic deformation to some extent despite the superior hardness. Motivated by this observation, it was attempted to predict the stress-strain curves for individual phase and overall microstructure using the nanoindentation tests data employing a model proposed in [19]. The predicted local stress-strain relations show that while the BCC

phase undergoes a strain hardening due to the applied load, the C_{14} Laves phase experiences continuous damage softening.

2. Materials and methods

2.1. Sample preparation

A homogenous non-equiatomic $Al_2CrFeMnTi$ high-entropy alloy was prepared via mechanical alloying (MA) using elemental powders with the purity of 99.9% and an average particle size of 45 μm. MA was carried out using a Restch^{TM} PM 200 high-speed planetary ball mill with a speed of 400 rpm for 10 hours in a stainless-steel vial using stainless steel balls with a diameter of 6.35 mm and the ball to powder weight ratio (BPR) of 10:1. The powders were loaded in the vials inside a glove box under an argon atmosphere to prevent oxidation during ball milling. It is worth mentioning that to achieve chemically homogamous powder alloy, the milling time, milling speed, and BPR values were optimized in a preliminary study.

The mechanically alloyed (MA'd) powder alloy subsequently melted inside an alumina crucible in an induction furnace under a high-purity argon atmosphere and then solidified inside the furnace. Application of MA before casting process can significantly reduce the time required for the alloying process at melting temperature and leads to obtaining a chemically homogeneous alloy in a very short time. The density of as-cast samples was measured to be about 98.5% using the Archimedes method in ethanol.

Table 1 reports the chemical composition of as-cast samples measured using the BrukerTM S8 TIGER X-Ray Fluorescence (XRF) technique, where the negligible difference with the nominal composition confirms that all the intended constituent elements are present in the composition.

Table 1. The chemical composition of the as-cast sample which was measured by XRF.

	Al		Cr		Fe		Mn		Ti	
	at%	wt%	at%	wt%	at%	wt%	at%	wt%	at%	wt%
Mixture powder	33.32	20.40	16.67	19.60	16.67	21.10	16.67	20.80	16.67	18.10
As-cast sample	32.71	19.95	16.81	19.75	16.42	20.72	17.01	21.13	17.05	18.45

2.2. Microstructural characterizations

As-cast samples were metallographically prepared using conventional grinding and polishing procedures to achieve a mirror-like surface finish. Microstructural analysis was carried out using scanning electron microscopy (SEM) images employing backscattered electron imaging

mode. The individual elemental analyses were measured using energy-dispersive X-ray spectroscopy (EDS) in SEM.

Phases identification in the MA'd powder and as-cast samples were carried out by analyzing X-ray diffraction patterns (XRD) taken in a Bruker™ D8 Advance X-ray diffractometer with Cu radiation target ($\lambda = 1.5405$Å).

Thermodynamic calculations were performed in CALPHAD software using the TCHEA3 database to obtain equilibrium phases in this quinary system and compared with the experimental data and X-ray diffraction patterns (XRD).

2.3. Mechanical testing

The mechanical properties, including hardness (H) and modulus of elasticity (E), were determined using the Oliver-Pharr method [20] by analyzing the loading and unloading curves obtained from nanoindentation tests. Nanoindentations are carried out using Agilent G200 instrument equipped with a diamond Berkovich indenter tip under the load-control mode. To determine local and the overall mechanical properties of the samples, two indentation load values of 10 mN and 300 mN with a loading rate of 1 and 30 mN/s, respectively, and loading time and dwell time of 10 and 5 seconds, respectively, were applied on the specified locations of the microstructure. The value of the Poisson's ratio was considered to be 0.3 for measurements of the individual phases and the entire cast alloy. Deviation of Poisson's ratio from this value will not significantly affect the indentation depth [21]. Load-displacement data was continuously recorded, and the values of the E and H were averaged over at least 15 measurements and reported with the associated standard deviations.

Since the Oliver-Pharr method cannot account for the pile-up effect on the measurements at the greater depth and loads, the residual indents traces made by applying 300 mN load were imaged using atomic force microscopy (AFM), Brucker, Dimension Icon in the tapping mode. The correction method [22] was explained in detail in the corresponding section. The stress-strain curves of individual phases and the overall flow curve of the material were calculated from nanoindentation results based on the method reported in [19].

3. Results and discussions

X-ray diffraction patterns of as-blended and MA'd powder are shown in Figures 1a & b. The individual elemental peaks in as-blended powder (Figure 1a) disappeared after the MA of the powder alloy (Figure 1b). The new reflections peaks illustrated in Figure 1b reveals that the crystal structure of the MA'd powder is BCC, with three characteristic peaks at $2\theta = 44.51$,

64.55, and 81.97° with a lattice constant calculated to be 0.2882 nm. The observed peak broadening and reduced intensity detected in Figure 1b are associated with the increment of strain and decreased crystallite size of MA'd powder alloy, as is also reported in [23]. It is already known that the elements with low melting points dissolve in the matrix with a higher melting point during the MA process [24, 25]. For the same reason, the MA'd powder of the $Al_2CrFeMnTi$ alloy forms a BCC crystal structure, despite having FCC-structured Al as a major element.
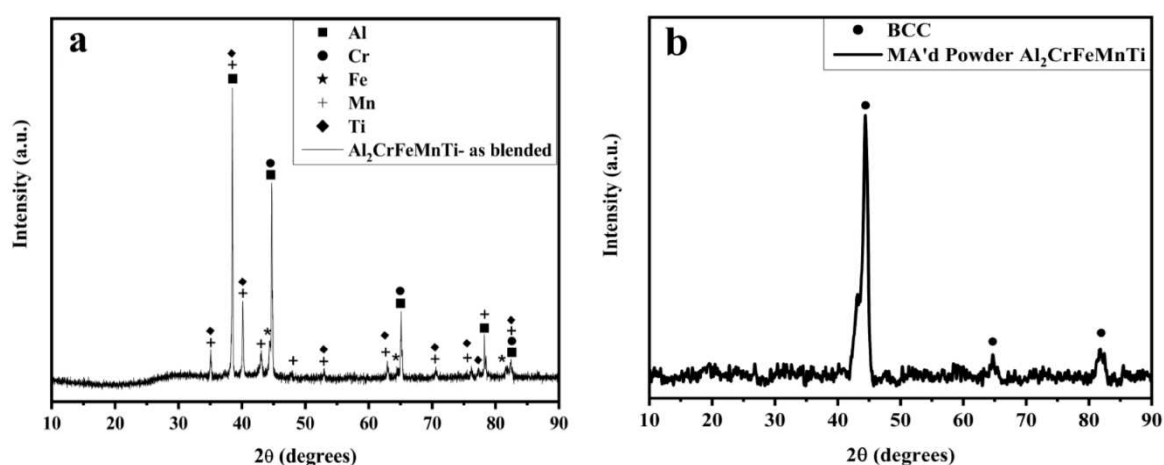

Figure 1. XRD patterns of (a) as-blended, (b) MA'd powder. By employing the mechanical alloying process, the individual elemental peaks in (a) are disappeared, and the characteristic peaks of a new BCC crystalline phase are observed in (b).

Figure 2a shows an SEM micrograph of the produced powder with the MA technique where the average particle size is measured to be in the range of 15-30 μm; this indicates a reduction in particle size compared to the initial size of the particles. The reduced particles' size after MA could be associated with the ball milling process since continuous fracture, cold welding, and re-welding processes take place [25]. The particles have nearly spherical morphology, with surfaces covered by layered topography. These layers drastically deform because of the repeated cold welding-fracture cycle of powders. During ball milling, continuous atomic diffusion occurs in these layers, which eventually results in the formation of solid-solution alloy powder [26]. The EDS spectrum in Figure 2b represents the chemical composition of a selected random powder, indicating that all the introduced elements to the powder exist in their intended quantity. Moreover, the EDS measurements show an identical distribution of the five elements in the powder particles with a negligible amount of O and C. Table 2 reports the average weight percentage of the elements taken from 15 measurements along with the standard deviations of

the average value. The composition of the MA's powder obtained from EDS spectra is in good agreement with the mixed weight fraction.
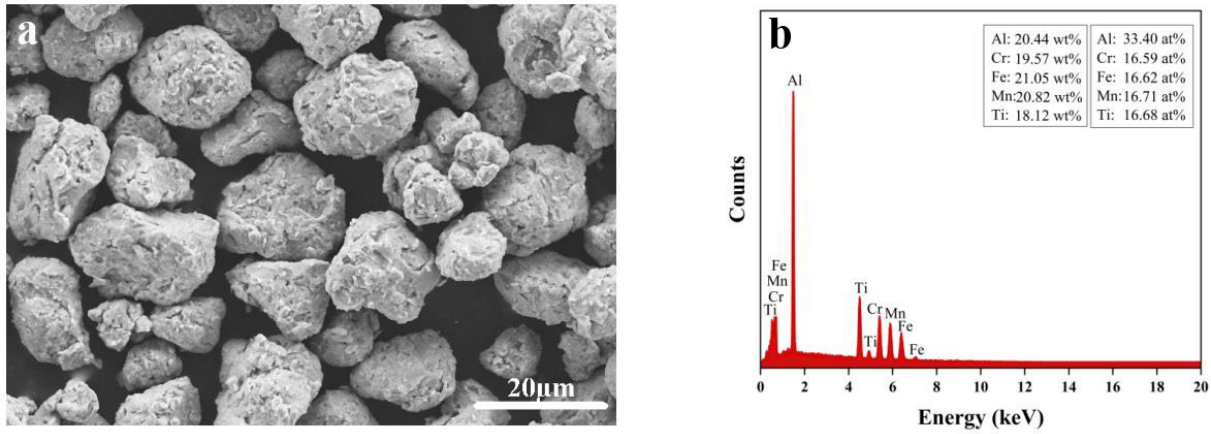

Figure 2. (a) SEM image of the MA'd powder, showing semi-spherical morphology of the particles. (b) An EDS spectrum was obtained from one particle with the identified elemental peaks.

Table 2. The measured chemical composition of the MA'd powder obtained by EDS compared with the nominal composition of the prepared powder mixture.

	Al (wt%)	Cr (wt%)	Fe (wt%)	Mn (wt%)	Ti (wt%)
Mixture powder	20.4	19.6	21.1	20.8	18.1
MA'd powder	21.4	19.2	20.8	21.0	18.0
Standard deviation	0.71	0.27	0.25	0.14	0.07

Figure 3a shows the results of thermodynamic calculations through Thermo-Calc, as explained in the microstructure characterization section. Based on Figure 3a, BCC and C_{14} phases are expected to be at equilibrium in the range of 500℃-1600℃, while $L2_1$ starts to precipitate at about 429℃ in expense of C_{14} phase.

The XRD spectrum of the bulk $Al_2CrFeMnTi$ as-cast alloy is shown in Figure 3b, where the identified peaks reveal the presence of the two crystalline phases of the BCC and C_{14}. The blue and red spectra show the fundamental peaks associated with the BCC and C_{14} phases, respectively. Although the BCC phase is expected to be the main phase according to the higher intensity of the obtained signal, no characteristic peaks related to the presence of the $L2_1$ phase are detected. This finding is most likely related to the meager $L2_1$ phase fraction in the as-cast samples consistent with the micrograph presented in Figure 4a. While the BCC phase has a lattice parameter of $a_{BCC} = 0.2968$ nm, the C_{14} phase has the HCP crystal structure with associate lattice parameters of $a_{C14} = 0.4951$ nm and $c_{C14} = 0.8039$ nm. According to Figure 3a, during

the equilibrium solidification of the Al$_2$CrFeMnTi alloy, the C$_{14}$ is the first phase to nucleate at about 1456 °C. As more liquid is solidified, the phase fraction of the C$_{14}$ phase increases, which continues until the onset of the BCC phase formation at 1400 °C. As it is shown in Figure 3a, the formation of the BCC phase is accompanied by a sudden reduction in the phase fraction of the C$_{14}$ phase that can be linked to the fact that both phases contain a similar distribution of Fe and Al. Therefore, the formation of the BCC at 1400 °C reduces the available Fe and Al solute atoms in the surrounding liquid. Such deficiency could hinder both nucleation of the new C$_{14}$ phase and growth of the existing ones. The precipitation process of the L2$_1$ phase starts after the complete solidification at 429 °C leading to a reduction in the C$_{14}$ phase fraction.
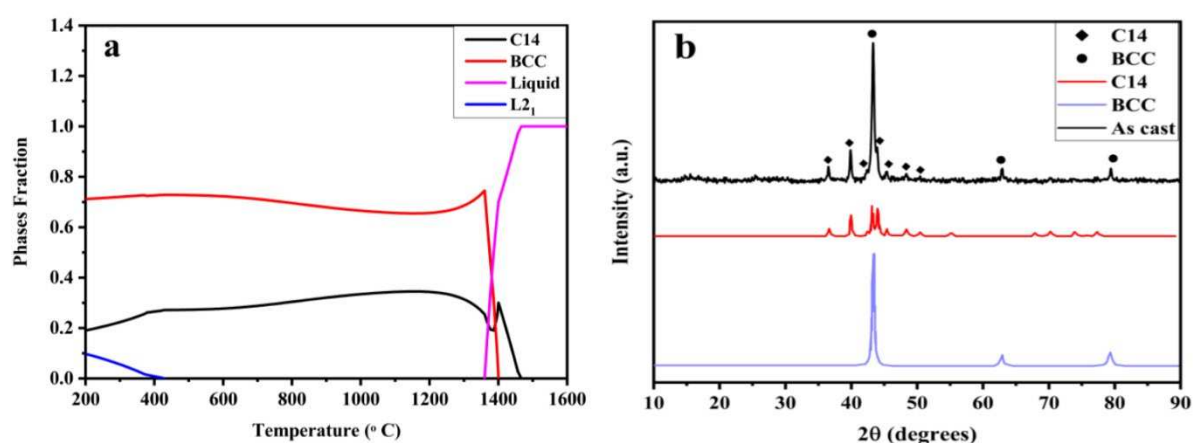

Figure 3. (a) Equilibrium phases' volume fraction of Al$_2$CrFeMnTi alloy as a function of temperature showing the formation of two phases upon solidification and one phase upon solid-state transformation. (b) XRD patterns of the as-cast sample, showing the corresponding peaks of the BCC and C$_{14}$ phases.

The micrograph of Figure 4a shows a typical microstructure obtained in the as-cast state of the Al$_2$CrFeMnTi alloy. The microstructure is composed of three phases: the BCC phase with a lighter color, the Laves C$_{14}$ phase having a darker color, and the L2$_1$ precipitate within the BCC phase. Therefore, the experimental equilibria phases in the current study are consistent with the thermodynamic calculations despite the rapid solidification during the employed casting process. There are two different morphologies of Laves C$_{14}$ phase within the microstructure, as highlighted in Figure 4 (a). The first type takes the larger fraction of the microstructure with irregular morphology, marked as C14^1 on the image, and the plate-like regions (*i.e.,* the second type) formed within the BCC phase with a higher aspect ratio is named C$_{14}$^{2}. The interphase boundary between C$_{14}$^{1} and BCC phase is highly serrated, which is believed to be due to a high cooling rate utilized in the casting process. Such a jagged interface is not observed for the C$_{14}$^{2} regions and the BCC islands in the microstructure. The formation of the C$_{14}$ phase within the

8

BCC phase was observed after heat treatment in $Al_{1.5}CrFeMnTi$ [18]; however, in the studied alloy having slightly higher Al, the formation of C_{14} phase within the BCC phase are frequently observed in as-cast samples.

The chemical content of BCC and C_{14} ($L2_1$ is excluded since ultrafine precipitates are not clearly detected) in Table 3 shows that there is a clear difference in the concentration of alloying elements, other than Al and Fe, with the BCC phase being enriched by Mn and Cr while C_{14}, regardless of being C_{14}^1 or C_{14}^2 type, shows a higher concentration of Ti.
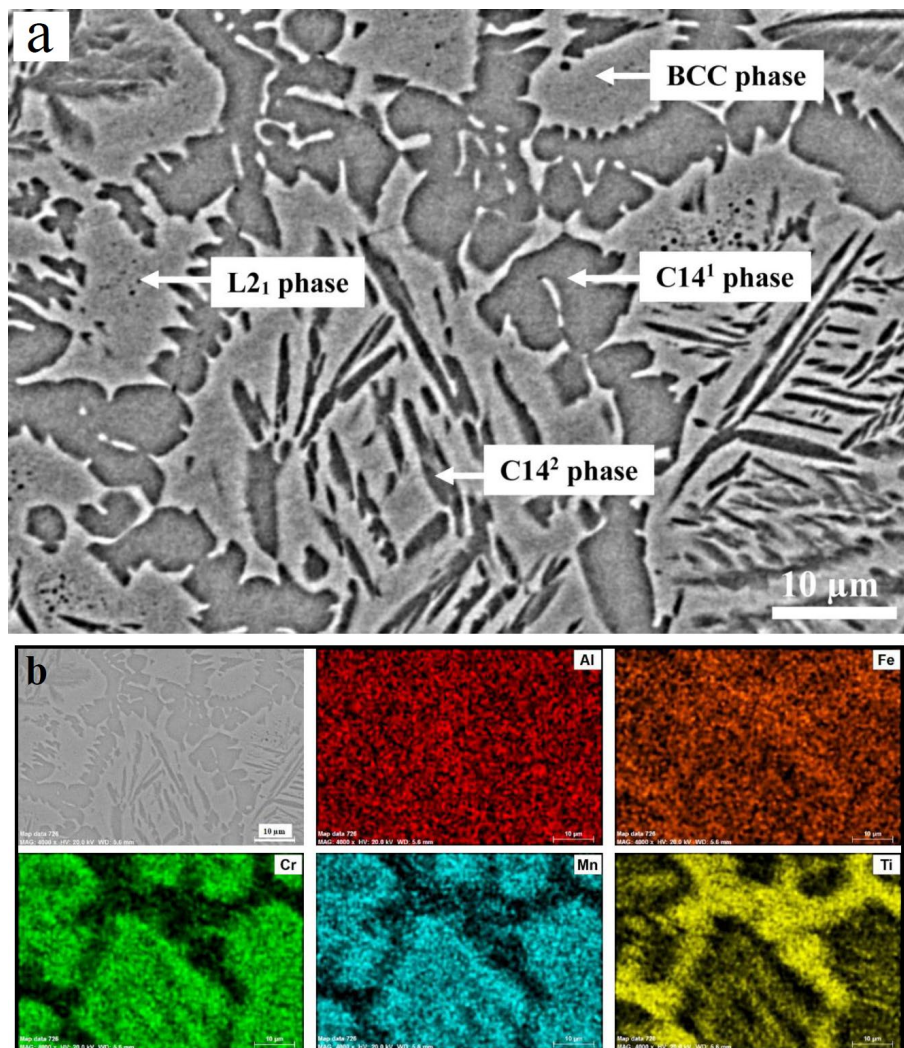

Figure 4. (a) The SEM micrograph and (b) EDS elemental mapping of as-cast $Al_2CrFeMnTi$ sample. The BCC phase has lighter color due to the presence of heavier elements, while the C_{14} phase has darker color in the BS-SEM image. A Low fraction of ultrafine $L2_1$ precipitates is observed within the BCC phase.

Table 3. Chemical composition of BCC and C_{14} phases obtained by EDS spot analysis.

	Al (wt%)	Cr (wt%)	Fe (wt%)	Mn (wt%)	Ti (wt%)
BCC	18.30	22.74	21.74	25.85	11.37
$C14^1$	18.67	10.42	24.86	14.82	31.23
$C14^2$	18.54	10.32	24.91	15.16	31.07

The local mechanical properties of the $Al_2CrFeMnTi$ alloy, *i.e.,* the hardness (H) and elastic modulus (E) of the individual BCC and C_{14} phases, were characterized using the nanoindentation technique with an applied load of 10 mN to ensure the indentation was carried out on the targeted phases. The indentation was performed in a 5×5 matrix, as illustrated in Figure 5a, where indents were 100 μm apart to minimize the effect of neighboring indentation and associated work-hardening on the results. SEM micrographs were used to determine the location of the individual indents with respect to the underlying microstructural phases; however, only indents located within a particular phase are evaluated, and indents at interfacial regions are not taken into consideration. An example of measured load-displacement curves is shown in Figure 5b, where the black and red curves represent the C_{14} and BCC phases, respectively. Since the experiments were conducted in the load control mode, the maximum applied force is identical for both phases. However, the measured displacements vary significantly, with a residual displacement of about 125 nm for the C_{14} and about 190 nm for the BCC phases measured after the load was released. The lower displacement in C_{14} shows that the phase resists more against the applied load and the resultant stresses with the hardness value of $H_{C14} = 14.86 \pm 0.12$ GPa, which is higher than $H_{BCC} = 8.91 \pm 0.10$ GPa. It is worth noting that several loading curves of the C_{14} phase exhibit minor pop-in event that is a typical phenomenon in load-displacement curves of Laves phases, mainly due to the localized plastic deformation and dislocation activity [27]. Compared to the typical hardness range of the BCC phase [28], a higher hardness value for the BCC phase in the developed alloy phases is observed, which could be linked to the presence of the ultra-fine $L2_1$ phase precipitates restricting the dislocation motion, and hence, it resists against the plastic deformation. Despite the considerable variation of hardness values, both phases show an almost identical modulus of elasticity ($E_{BCC} = 256.2 \pm 5.3$ GPa and $E_{C14} = 254 \pm 4.9$ GPa).
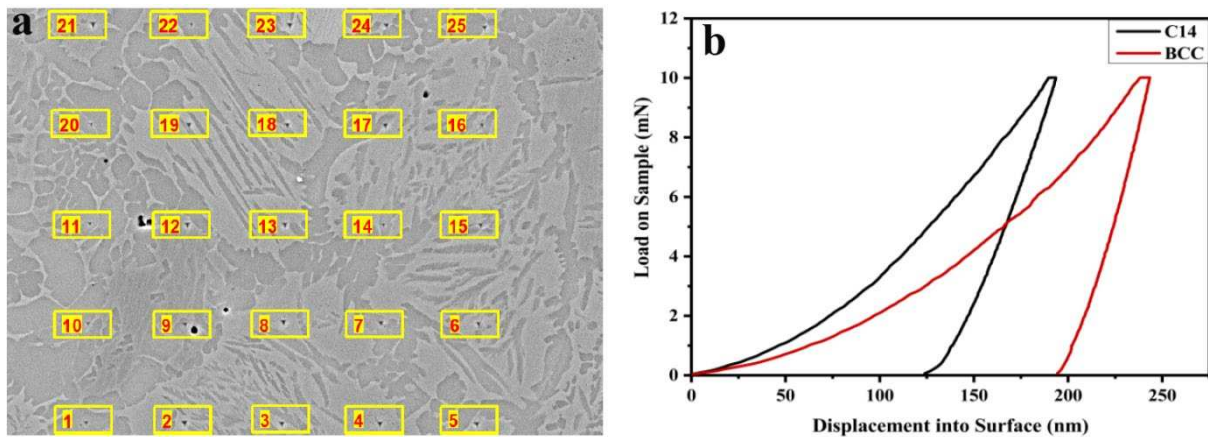
Figure 5. (a) SEM micrograph of indent marks imprinted on the constituent phases and (b) loading-displacement curves for the BCC and C_{14} phases.

In order to measure the overall hardness of the alloy, 20 indentations were performed by applying a constant load of 300 mN. Such high applied load increased the footprint and subsequent subsurface interaction volume of the indenter. Therefore, a more extensive section of the material will respond to the applied load that would determine the alloy's overall hardness. Figure 6a illustrates a single indent trace and the corresponding load-displacement curve in Figure 6b. Close examination of the trace of indent captured by AFM image revealed that the edges of the indents are semi-convex (Figure 6c). Accordingly, a larger surface area would contact the indenter because of pile-up, leading to the overestimation of H and E values. Thus, the method described by Kese et al. [22] is employed to account for the pile-up effect. Three lines, each passing through the corners of the triangular indent trace and the midpoint of the opposite edge, were scanned. The variations in pile-up heights were plotted as I, II, and III profiles, as shown in Figure 6d, with the height and width of the pile-up being more pronounced on two sides of the indent mark. The values of H and E were adjusted by quantifying the effect of the pile-up. The H_{ave} and E_{ave} values, before and after this correction, are reported in Table 4. It is known that the formation of significant pile-ups is correlated to the elastic and plastic deformations of material under the applied load. Although the reduction in H value (5% decrease caused by pile-up) of the studied alloy is not very high, the formation of great amounts of pile-up in such microstructure with a considerable fraction of Laves phase is significant. In addition, no (macro) cracks are observed under severe loading, denoting that the alloy exhibits some ductility even at room temperature.
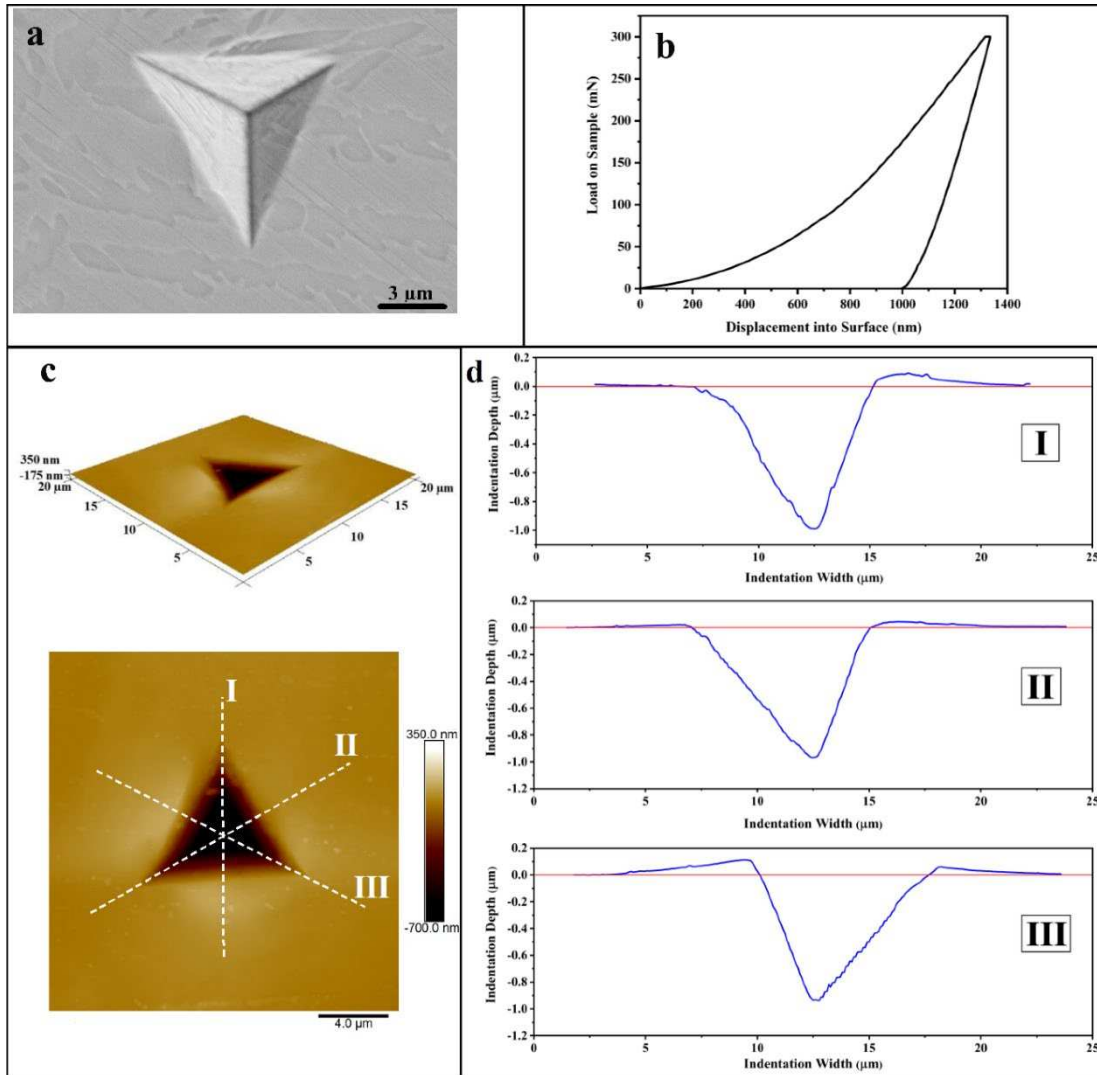
Figure 6. (a) A trace of indent on the microstructure, including all three phases. (b) The load-displacement curve was obtained by applying 300 mN load. (c) 3D and 2D traces of an indent were observed in AFM. (d) Three scanning lines, shown by I, II, and II, show variations in height due to pile-up in the scanned positions.

Table 4. The values of average hardness and average modulus of elasticity of the alloy.

Before pile-up correction		After pile-up correction	
H (GPa)	E (GPa)	H (GPa)	E (GPa)
8.3±0.4	203±5.1	7.9±0.3	198±4.2

Force-displacement curves obtained from nanoindentation tests were further analyzed to calculate the stress-strain curve of the individual C_{14} and BCC phases as well as the overall stress-strain curve of the alloy, which includes all three phases. When an elastoplastic material is subjected to a sharp indentation, the mechanical response can be described by Kick's law, $P = Ch^2$, where P, h, and C are indentation load, indentation depth, and the curvature of the loading

12

curve, respectively, as explained in [19]. Figure 7a illustrates the predicted stress-strain curves for the BCC and C_{14} phases (considering that the BCC phases contain $L2_1$ precipitates). The stress-strain curve of the BCC phase, with square markers, exhibits typical behavior of the elastoplastic material with a yield stress of about 1900 MPa. Nevertheless, the behavior of the C_{14} phase with circular marker does not follow the expected behavior for a ductile material as the flow stress is consistently dropping by applied strain, and hence, the increment of the indenter penetration. The error bars in both curves demonstrate the standard error of calculated flow stress values of each indent within the individual phase. On the other hand, the stress-strain curve obtained from the high load of 300 mN (Figure 7b) predicts a considerable amount of strain, indicating the alloy undergoes plastic deformation. This finding is consistent with observed pile-ups around the indent trace shown in Figure 6c. Therefore, the mechanical response of the current alloy can be described by these main mechanisms: solid solution and strain hardening mostly related to the BCC phase, precipitation hardening associated with the $L2_1$ phase, and strengthening due to the presence of a large amount of the interphase boundaries.
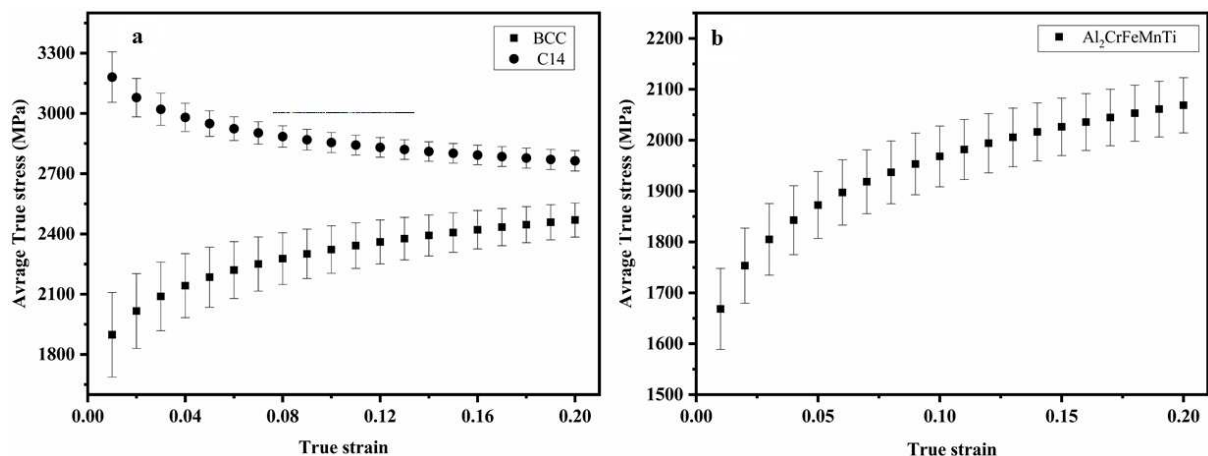

Figure 7. Calculated stress-strain curves using nanoindentation test data (a) stress-strain curve of individual phases obtained by applying 10 mN load and (b) stress-strain curve of overall microstructure obtained by applying 300 mN load on the three phases.

Conclusion

$Al_2CrFeMnTi$ light-weight high entropy alloy was successfully synthesized via mechanical alloying with the subsequent casting process. Key findings were obtained from the present work are as follows:

- Analyzing the XRD patterns shows that while in the MA'd powder alloy, only the peaks of the BCC phase appeared, diffraction patterns of the as-cast samples contained peaks

of both BCC and C_{14} phases. The phase formation in as-cast samples is consistent with the CALPHAD results even though the phase fractions deviate significantly.

- The microstructure of $Al_2CrFeMnTi$ alloy consists of the solid-solution BCC phase, the C_{14} Laves intermetallic, and ultra-fine $L2_1$ precipitates.

- The existence of two intermetallic phases together with the BCC phase increased the hardness of the alloy, 7.9 ± 0.3 GPa, obtained from nanoindentation tests after applying the pile-up correction. Despite this superior hardness and the expected brittleness, no cracks were observed around the intent marks. The alloy undergoes a moderate strain as a response to the applied load. This behavior is consistent with the observation of pile-up around the indent marks. Therefore, it is proposed that the mechanical behavior of the multiphase $Al_2CrFeMnTi$ alloy is affected by several mechanisms: solid solution and strain hardening imposed by the BCC phase, precipitation hardening due to $L2_1$ precipitates, and hardening caused by the large surface area associated with interphase boundaries.

The superior mechanical properties of $Al_2CrFeMnTi$ alloy combined with its reduced weight and cost indicate a high potential for wear-resistant and high-temperature applications. The utilization of this alloy for industrial applications requires further investigations on its high-temperature performance. Additionally, understanding the variations in microstructure and the structure-dependent properties under different manufacturing techniques is of great value. Moreover, comprehensive mechanical characterizations, such as compression, tensile, and fatigue testing, are required to thoroughly analyze this alloy's mechanical properties. Complementary studies on these subjects are being conducted to gain further insight into the relationship between fabrication process/microstructure/properties in Al and Ti-based light-weight high entropy alloys.

Reference

[1] B. Cantor, I. T. H. Chang, P. Knight, and A. J. B. Vincent, Microstructural development in equiatomic multicomponent alloys, Materials Science and Engineering: A, 375-377 (2004) 213-218. https://doi.org/10.1016/j.msea.2003.10.257

[2] Y. F. Ye, Q. Wang, J. Lu, C. T. Liu, and Y. Yang, High-entropy alloy: challenges and prospects, Materials Today, 19 (2016) 349-362. https://doi.org/10.1016/j.mattod.2015.11.026

[3] D. B. Miracle and O. N. Senkov, A critical review of high entropy alloys and related concepts, Acta Materialia, 122 (2017) 448-511. https://doi.org/10.1016/j.actamat.2016.08.081

[4] I. Toda-Caraballo and P. E. J. Rivera-Díaz-del-Castillo, Modelling solid solution hardening in high entropy alloys, Acta Materialia, 85 (2015) 14-23. https://doi.org/10.1016/j.actamat.2014.11.014

[5] J.-W. Yeh, Physical Metallurgy of High-Entropy Alloys, JOM, 67 (2015) 2254-2261. https://doi.org/10.1007/s11837-015-1583-5

[6] I. Basu and J. T. M. De Hosson, Strengthening mechanisms in high entropy alloys: Fundamental issues, Scripta Materialia, 187 (2020) 148-156. https://doi.org/10.1016/j.scriptamat.2020.06.019

[7] K. S. Tun, P. Murugan, T. S. Srivatsan, and M. Gupta, Synthesis and Characterization of aluminium based multicomponent alloys, Materials Today: Proceedings, 46 (2021) 1210-1214. https://doi.org/10.1016/j.matpr.2021.02.066

[8] N. Takata, H. Ghassemi Armaki, Y. Terada, M. Takeyama, and K. S. Kumar, Plastic deformation of the C14 Laves phase (Fe,Ni)2Nb, Scripta Materialia, 68 (2013) 615-618. https://doi.org/10.1016/j.scriptamat.2012.12.019

[9] D. Choudhuri, B. Gwalani, S. Gorsse, M. Komarasamy, S. A. Mantri, S. G. Srinivasan, R. S. Mishra, and R. Banerjee, Enhancing strength and strain hardenability via deformation twinning in fcc-based high entropy alloys reinforced with intermetallic compounds, Acta Materialia, 165 (2019) 420-430. https://doi.org/10.1016/j.actamat.2018.12.010

[10] Z. G. Wang, W. Zhou, L. M. Fu, J. F. Wang, R. C. Luo, X. C. Han, B. Chen, and X. D. Wang, Effect of coherent L12 nanoprecipitates on the tensile behavior of a fcc-based high-entropy alloy, Materials Science and Engineering: A, 696 (2017) 503-510. https://doi.org/10.1016/j.msea.2017.04.111

[11] M. Wang, H. Cui, Y. Zhao, C. Wang, N. Wei, Y. Zhao, X. Zhang, and Q. Song, A simple strategy for fabrication of an FCC-based complex concentrated alloy coating with hierarchical nanoprecipitates and enhanced mechanical properties, Materials & Design, 180 (2019) 107893. https://doi.org/10.1016/j.matdes.2019.107893

[12] M. Wang, Y. Lu, T. Wang, C. Zhang, Z. Cao, T. Li, and P. K. Liaw, A novel bulk eutectic high-entropy alloy with outstanding as-cast specific yield strengths at elevated temperatures, Scripta Materialia, 204 (2021) 114132. https://doi.org/10.1016/j.scriptamat.2021.114132

[13] R. Feng, M. C. Gao, C. Lee, M. Mathes, T. Zuo, S. Chen, J. A. Hawk, Y. Zhang, and P. K. Liaw, Design of Light-Weight High-Entropy Alloys, Entropy, 18 (2016) 1-21. https://doi.org/10.3390/e18090333

[14] O. Stryzhyboroda, V. T. Witusiewicz, S. Gein, D. Röhrens, and U. Hecht, Phase equilibria in the Al–Co–Cr–Fe–Ni high entropy alloy system: thermodynamic description and experimental study, Frontiers in Materials, 7 (2020) 1-13. https://doi.org/10.3389/fmats.2020.00270

[15] Y. Lu, Y. Dong, H. Jiang, Z. Wang, Z. Cao, S. Guo, T. Wang, T. Li, and P. K. Liaw, Promising properties and future trend of eutectic high entropy alloys, Scripta Materialia, 187 (2020) 202-209. https://doi.org/10.1016/j.scriptamat.2020.06.022

[16] S. Liu, M. C. Gao, P. K. Liaw, and Y. Zhang, Microstructures and mechanical properties of AlxCrFeNiTi0.25 alloys, Journal of Alloys and Compounds, 619 (2015) 610-615. https://doi.org/10.1016/j.jallcom.2014.09.073

[17] K. Zhang and Z. Fu, Effects of annealing treatment on phase composition and microstructure of CoCrFeNiTiAlx high-entropy alloys, Intermetallics, 22 (2012) 24-32. https://doi.org/10.1016/j.intermet.2011.10.010

[18] R. Feng, M. C. Gao, C. Zhang, W. Guo, J. D. Poplawsky, F. Zhang, J. A. Hawk, J. C. Neuefeind, Y. Ren, and P. K. Liaw, Phase stability and transformation in a light-weight high-entropy alloy, Acta Materialia, 146 (2018) 280-293. https://doi.org/10.1016/j.actamat.2017.12.061

[19] M. Dao, N. Chollacoop, K. J. Van Vliet, T. A. Venkatesh, and S. Suresh, Computational modeling of the forward and reverse problems in instrumented sharp indentation, Acta Materialia, 49 (2001) 3899-3918. https://doi.org/10.1016/S1359-6454(01)00295-6

[20] W. C. Oliver and G. M. Pharr, An improved technique for determining hardness and elastic modulus using load and displacement sensing indentation experiments, Journal of Materials Research, 7 (1992) 1564-1583. https://doi.org/10.1557/JMR.1992.1564

[21] W. Yan, C. L. Pun, and G. P. Simon, Conditions of applying Oliver–Pharr method to the nanoindentation of particles in composites, Composites Science and Technology, 72 (2012) 1147-1152. https://doi.org/10.1016/j.compscitech.2012.03.019

[22] K. O. Kese, Z. C. Li, and B. Bergman, Method to account for true contact area in soda-lime glass during nanoindentation with the Berkovich tip, Materials Science and Engineering: A, 404 (2005) 1-8. https://doi.org/10.1016/j.msea.2005.06.006

[23] Y. C. Liao, T. H. Li, P. H. Tsai, J. S. C. Jang, K. C. Hsieh, C. Y. Chen, J. C. Huang, H. J. Wu, Y. C. Lo, C. W. Huang, and I. Y. Tsao, Designing novel light-weight, high-strength and high-plasticity Tix(AlCrNb)100-x medium-entropy alloys, Intermetallics, 117 (2020) 106673. https://doi.org/10.1016/j.intermet.2019.106673

[24] W. Chen, Z. Fu, S. Fang, H. Xiao, and D. Zhu, Alloying behavior, microstructure and mechanical properties in a FeNiCrCo0.3Al0.7 high entropy alloy, Materials & Design, 51 (2013) 854-860. https://doi.org/10.1016/j.matdes.2013.04.061

[25] I. Moravcik, J. Cizek, P. Gavendova, S. Sheikh, S. Guo, and I. Dlouhy, Effect of heat treatment on microstructure and mechanical properties of spark plasma sintered AlCoCrFeNiTi0.5 high entropy alloy, Materials Letters, 174 (2016) 53-56. https://doi.org/10.1016/j.matlet.2016.03.077

[26] C. Suryanarayana, Mechanical alloying and milling, Progress in Materials Science, 46 (2001) 1-184. https://doi.org/10.1016/S0079-6425(99)00010-9

[27] Y. X. Ye, Z. P. Lu, and T. G. Nieh, Dislocation nucleation during nanoindentation in a body-centered cubic TiZrHfNb high-entropy alloy, Scripta Materialia, 130 (2017) 64-68. https://doi.org/10.1016/j.scriptamat.2016.11.019

[28] M.-H. Tsai and J.-W. Yeh, High-Entropy Alloys: A Critical Review, Materials Research Letters, 2 (2014) 107-123. https://doi.org/10.1080/21663831.2014.912690